

# Lower-Hybrid Drift Instability and Macroscopic Flow of Colliding Magnetized Plasmas

M.A. Malkov<sup>1</sup>, V.I. Sotnikov<sup>2</sup>

<sup>1</sup>*CASS and Department of Physics, University of California, San Diego, La Jolla, CA 92093*

<sup>2</sup>*Air Force Research Laboratory, Sensors Directorate, WPAFB, OH 45433*

Microscopic instability and macroscopic flow pattern resulting from colliding plasmas are studied analytically in support of laboratory experiments. The plasma flows are assumed to stream radially from two separate centers. In a quasi-planar (2D) geometry, they may arise from an Ohmic explosion of two parallel wires, but similar configurations emerge from other outflows, e.g., colliding winds in binary star systems. One objective of this paper is to characterize the flow instabilities developing near the flow stagnation line. An exact solution for the Buneman-type dispersion equation is obtained without conventional simplifications. The unstable wave characteristics are key to anomalous resistivity that determines the reconnection rate of opposite magnetic fields transported with each flow toward the stagnation zone. The second objective of the paper is to calculate the stream function of the plasma shocked upon collision. We addressed this task by mapping the flow region to a hodograph plane and solving a Dirichlet problem for the stream function. By providing the instability growth rate, responsible for anomalous transport coefficients, and the overall flow configuration, these studies lay the ground for the next step. From there, we will examine the field reconnection scenarios and emerging mesoscopic structures, such as radial striata observed in the experiments.

## I. INTRODUCTION

Colliding plasma flows with nearly opposite magnetic field orientation, often supersonic and superalfvenic, is an exciting and challenging problem to study. It has numerous applications in laboratory and space plasmas. The list of relevant systems includes, but is not limited to, colliding winds from two neighboring stars (often called binaries), corotating interaction regions in a solar wind plasma near the ecliptic plane, flows associated with the coronal mass ejection from the Sun, or even wall reflected counterpropagating plasma stream in hybrid and PIC simulations of collisionless shocks. In laboratory plasmas, one of the simplest configurations leading to colliding plasma flows can be created by driving strong unidirectional currents through a pair of parallel wires. The azimuthal magnetic fields generated around each wire, and the Ohmic current dissipation and heating occurring upon wire evaporation, launches strong radial outflows of magnetized plasmas. Upon colliding with each other, they form a flow pattern highly suggestive of magnetic field reconnection, and the development of various plasma instabilities, Figs. 1 and 2. Indeed, the symmetry plane between the wires must be the place where magnetic field lines from the opposing flows reconnect, Fig.2, as they need to conform to a single circular field configuration at distances much larger than the gap between the wires.

The reconnection efficiency strongly depends on the flow dissipation rate in the reconnection zone. In the case of hot outflows not significantly cooled by expansion, or even additionally heated upon their interaction with each other, the plasma binary collisions remain rare. In this case the anomalous resistivity, supported by plasma micro-instabilities that are likely to develop in the flows, takes the role of the classical resistivity. The potential of the flows to drive strong instabilities is the first topic of this paper. Knowing their growth rates and how are they distributed in the flow collision zone will allow one to understand the overall flow organization. These two sides of the problem are strongly related and should be treated on an equal footing which is, however, a formidable task. Therefore, our strategy consists of determining the instability growth rate making only most general assumptions about the flow and wave

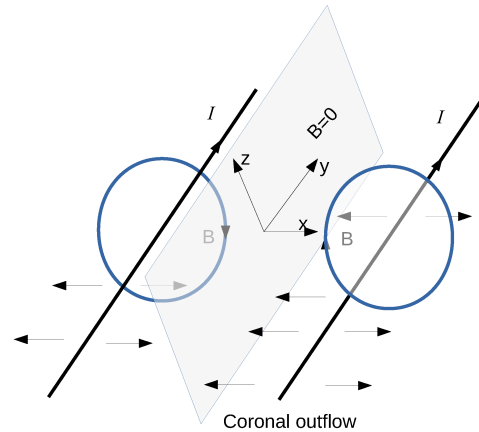


Figure 1. Schematics of the experimental setup. Two wires, carrying current  $I$  each, are directed along the  $y$ - axis and connect the chamber electrodes (not shown).

parameters. In particular, selecting the lower-hybrid drift instability (LHDI) as the most potent one to support the anomalous transport, we calculate its local growth rate with no further approximations. In other words, we solve the well-known dispersion relation for the LHDI (or any other two-stream type instability for that matter) exactly. In certain plasma flows, however, particularly some of the laser-evaporated target flows, there is no much room or time for the development of plasma micro-instabilities. With this regard, we refer the reader to the paper [14], where such colliding plasma flows with strong intraflow collisions have been studied in detail.

The second topic of the paper concerns the flow pattern emerging upon collision of outflows from two parallel wires. As in the instability part of our study, our strategy here is to calculate the stream function of the flow making only the most general assumptions about its character. One such assumption is the *insignificant* dynamic role of the magnetic field. This simplification, supported by experiments [16], allows us to calculate the stream function of colliding flows between two shocks formed upon collision using gas-dynamic rather than magnetohydrodynamic equations. As our research of the both topics is performed within a fairly general framework, we are planning to combine them to describe the flow collision phenomenon, followed by the magnetic energy dissipation through reconnection supported by the anomalous resistivity. Again, in the paper [14], an alternative situation of colliding MHD flows has been addressed with a primary emphasis on the magnetic aspect of the flow.

The paper is organized according to the following sections. Sec.II discusses the overall properties of the colliding flows. It further deals with the derivation of the dispersion relation for the LHDI and its closed form solution. Sec.III presents a more elaborate treatment of the post-shock flow based on a hodograph map of its area and derivation of the Chaplygin equations. The general solution for the stream function is presented. The equations for the parameters of the maps are given in Appendices. For illustration, a simplified flow example is also given. The paper concludes with a brief discussion of its topics, the summary main results, and an outline of the next steps.

## II. A MODEL FOR COLLIDING PLASMA FLOWS

### A. Sketch Description of the Flow

Before the two plasma flows reach a magnetic null ( $B \approx 0$ ), where they collide, partly interpenetrate and spread sideways, each of them undergoes a substantial evolution. This part of the problem has already been considered by others using a single wire setup (see, e.g., [16] and references therein). Many efforts have been made in conjunction with  $z$ -pinches. According to a universally accepted picture, the wire explosion can be broken down roughly into the following two phases.

Initially, most of the current between the electrodes flows through the wire that undergoes a complicated process of melting and vaporization. The details of these phenomena are, however, not so important for the present study. Next, when the plasma is created from the evaporated wire material and heated significantly, it forms an expanding *corona*. During this process, the current jumps from the wire to the corona. Some important physical phenomena occurring during the corona expansion, have been discussed and simulated, primarily within various MHD models [2, 16]. However, it has also been realized that some micro-physics not captured by the MHD approach is crucial to the macroscopic behavior of the corona. In particular, as the corona is rarefied and hot, it can transition into a collisionless regime. In this case, the macroscopic transport properties must be anomalous.

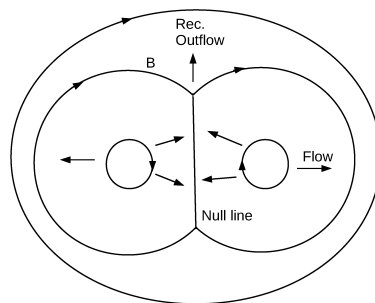


Figure 2. Reconnection flow initiated by parallel (out of plane) currents.

Turning to the double-wire configuration, there is no shortage of free energy sources for various instabilities that may play their parts in momentum and energy exchange between particles in each flow and between the colliding plasmas as a whole. So, the classical Spitzer resistivity needs to be complemented, if not replaced, by the anomalous one. A notably efficient instability, which in many cases has the lowest threshold, is the lower-hybrid drift instability (LHDI). While this instability has already been argued [1] to play an important role in a single-wire plasma expansion, we will study it in an environment created by two colliding coronal plasmas in the vicinity of the neutral plane. We will also significantly generalize the existing results by solving the LHDI dispersion equation exactly.

## B. General Dispersion Equation for the LHDI Instability

Strictly speaking, the system under consideration cannot be subjected to the conventional stability analysis starting from an equilibrium plasma state since the flow is time-dependent. However, as the LHDI is usually very fast, we may assume that the flow remains quasi-stationary over the instability e-folding time. Turning to the spatial scales of the problem we note that plasma is essentially inhomogeneous in at least two dimensions perpendicular to the wire direction. At the same time, the maximum growth rate is reached at scales comparable to, or even slightly smaller than, the electron gyroradius,  $\rho_e$ . The latter is, in turn, much smaller than all relevant scales (except the Debye length) associated with the plasma and magnetic field inhomogeneity. Therefore, we carry out the stability analysis based on a local approximation. We will use a coordinate system with the  $x$ -axis running normally to the wires in their plane,  $y$ -parallel to the wires and  $z$  will then be the vertical off-plane axis, Fig.1.

Based on the above considerations, the ion gyroradius strongly exceeds the characteristic wavelength of the instability, and the ion gyrofrequency is also much smaller than the growth rate. We will, therefore, treat ions as unmagnetized. Because of the electric field  $E_y$ , we include the ion drift velocity component in  $y$ -direction,  $V_{di} \sim \sqrt{eE_y y/M}$ .  $E_y$  is, however, not the only electric field component present in the plasma near the neutral plane. Due to effects of charge separation in colliding plasmas, associated primarily with the different gyroradii of electrons and ions, the  $E_x$  component must be quite strong. In addition, the two colliding plasmas may partially interpenetrate which should also build up electric field,  $E_x$ . More importantly, it will lead to an electron  $E \times B$  drift in the direction of wave propagation, that is,  $V_{Ey} \sim cE_x/B$ . We neglect the electron motion in  $z$  direction, assuming that  $k_z V_{ze} \ll k_y V_{ye}$ ,  $\omega$ . It is worth noting, however, that for sufficiently large  $k_z$ , the phase velocity of oscillations in  $z$ -direction,  $(\omega - k_y V_{ye})/k_z$ , may approach the electron thermal velocity which would result in a fast electron acceleration along the magnetic field. The field is oriented parallel to  $z$ -axis in the plane of the wires, but it is globally circular as it originates from the currents flowing through the wires.

Using a local approximation, we test stability of the following perturbation,  $\propto \exp(-i\omega t + ik_y y + ik_z z)$ , assuming also that  $k_z \ll k_y$ . The  $x$ -structure of the mode is ignored, as usual in the local approximation. In  $y$ - and  $z$ -directions, the plasma is considered to be homogeneous, even though the ion drift velocity, for example, slowly depends on  $y$ . Regarding the  $z$ -dependence, this approximation is valid not far away from the plane  $z = 0$ . We assume of course that  $L_y k_y \gg 1$ , where  $L_y$  is the size of the chamber in wire direction. Also, the presence of ion-neutral collisions should bring the ion drift velocity in the electric field direction to equilibrium, so the approximation of constant velocity appears plausible for the short-wave instability. There are also electron and ion drifts and currents, associated with the magnetic field, temperature and density variations in the  $x$ -direction that in general need to be included in the electron and ion responses to the wave perturbation.

A sufficiently general dispersion equation for the LHDI in electrostatic approximation, after obvious modifications suggested by our discussion above, can be adopted from, e.g. Ref. [3]:

$$1 + \frac{2\omega_{pi}^2}{k_y^2 V_{Ti}^2} [1 + \xi Z(\xi)] + \frac{\omega_{pe}^2}{\omega_{ce}^2} \frac{1 - I_0(b) e^{-b}}{b} - \frac{k_z^2}{k_y^2} \frac{\omega_{pe}^2}{(\omega - k_y V_{ye})^2} + \frac{2\omega_{pe}^2}{k_y^2 V_{Te}^2} \frac{k_y V_{\Delta}}{\omega - k_y V_{ye}} = 0 \quad (1)$$

Here we have used the following notations,

$$\xi = \frac{\omega - k_y V_{di}}{|k_y| V_{Ti}}, \quad Z(\xi) = -e^{-\xi^2} \left( 2 \int_0^{\xi} e^{z^2} dz - i\sqrt{\pi} \right), \quad b = \frac{|k_y| V_{Te}}{\omega_{ce}}$$

$$V_{\Delta} = -\frac{V_{Te}^2}{\omega_{ce}} I_0(b) e^{-b} \{ \kappa_n - \kappa_B [1 - b(1 - I_1/I_0)] - \kappa_T (1 - I_1/I_0) \},$$

where  $I_{0,1}$  are the modified Bessel functions,  $\kappa$ 's are the inverse scales of respective inhomogeneity,  $\kappa_n = n^{-1} dn/dx$ ,  $\kappa_B = B^{-1} dB/dx$ , and  $\kappa_T = T_e^{-1} dT_e/dx$ .

As we emphasized, in a flow resulting from the collision of two expanding plasmas the main instability driver is likely to be a relative motion of electrons and ions in the direction of wave propagation, that is, along the  $y$ -axis. Therefore, to determine the most favorable conditions for the instability, we may neglect the contributions of particle drifts associated with the inhomogeneity, collected in the term  $V_{\Delta}$ . We will also simplify the dispersion equation somewhat further using the following dimensionless variables

$$\hat{\omega} = \frac{\omega}{|k_y| V_{Ti}}, \quad \eta = \frac{\omega_{pi}^2}{k_y^2 V_{Ti}^2}, \quad \Omega_i = \frac{V_{di}}{V_{Ti}} \frac{k_y}{|k_y|}, \quad \Omega_e = \frac{V_{ey}}{V_{Ti}} \frac{k_y}{|k_y|}$$

Since we expect the relative bulk motion of electrons and ions to be the main driver of the instability, we neglect the thermal ion spread as well. The latter simplification translates into the condition  $|\xi| \gg 1$  and the dispersion equation rewrites

$$\mathcal{F}(\hat{\omega}) \equiv \frac{1}{(\hat{\omega} - \Omega_i)^2} + \frac{K}{(\hat{\omega} - \Omega_e)^2} = \frac{1}{\eta} + \frac{T_i}{T_e} b (1 - I_0(b) e^{-b}) \equiv A \quad (2)$$

where

$$K = (M/m) (k_z/k_y)^2 \quad (3)$$

Thus, we arrived at a fourth order algebraic equation for the frequency  $\hat{\omega}$ . Apart from the notation, the same equation is widely used in studies of Buneman and modified two-stream instabilities, e.g. [3, 9]. Of course, it can be solved exactly for  $\hat{\omega}$  using one of the solutions obtained by Ferrari, Euler and some other famous mathematicians of the past. At the same time, these solutions are quite laborious and impractical to use. ‘‘Mathematica,’’ for example, returns a set of four solutions filling the entire computer screen. Not surprisingly, equations similar to eq.(2) are usually solved either approximately or numerically. The numerical solutions will not be helpful in analytic calculations of the anomalous transport coefficients that are crucial for obtaining the macroscopic flow. The approximate solutions, on the other hand, are highly restrictive in situations where the flow is not known beforehand.

Indeed, our goal is to characterize the instability for the flow conditions changing arbitrarily in time and space. Also, a macroscopic back reaction of the developing instability on the flow itself will result in such changes. Therefore, it is highly desirable to obtain an exact solution to eq.(2) that would cover the entire parameter space without restrictions. We tackle this problem in the next subsection and demonstrate that such solution can, in fact, be quite manageable, by contrast to the full algebraic solution of the quartic eq.(2). The novelty of our approach is in that we separate the two complex roots from the two real roots, thus simplifying the solution tremendously.

### C. Instability Analysis

Let us start with summarizing simple and well-known aspects of eq.(2). First, as  $A > 0$ , two of the four solutions are purely real. They have the maximum and minimum real parts among the four solutions. The remaining two roots, which are between the poles at  $\hat{\omega} = \Omega_{e,i}$ , are also real if  $A - \mathcal{F}_{\min} > 0$ . The interesting case is when they are complex conjugate, that is when  $A - \mathcal{F}_{\min}(\hat{\omega}) < 0$ . One of the roots corresponds then to a positive growth rate  $\hat{\gamma} = \Im\hat{\omega}$ . This unstable root can be easily found near the instability threshold:

$$\Im\hat{\omega} \equiv \hat{\gamma} = \frac{4\delta^2 K^{1/6}}{\sqrt{3} (1 + K^{1/3})^{5/2}} \sqrt{\mathcal{F}(\hat{\omega}_0) - A}$$

Here  $\delta = (\Omega_e - \Omega_i)/2$  (assumed positive), and  $\hat{\omega}_0$  is where  $\mathcal{F}$  has a minimum,  $\Omega_i < \hat{\omega}_0 < \Omega_e$ . There are a few other limiting cases of eq.(2) that are frequently considered. For  $K = 1$ , one obtains a simple exact result when the equation can be transformed to a biquadratic form. In other cases, such as large or small  $K$ , the equation is treated only approximately.

Our goal, however, is to obtain exact expressions for both the frequency and the growth rate of unstable waves depending on parameters. As these are coordinate dependent, this will locate the wave generation domain, and therefore that of the current and flow dissipation. To this end, we simplify eq.(2) by reducing the number of parameters it depends on, from four to two. By introducing a new dimensionless frequency

$$\Omega = \frac{\hat{\omega}}{\delta} - \frac{1}{2\delta} (\Omega_i + \Omega_e) \quad (4)$$

and denoting  $B = \delta^2 A$ , eq.(2) rewrites

$$\frac{1}{(\Omega + 1)^2} + \frac{K}{(\Omega - 1)^2} = B \quad (5)$$

The parameter  $B$  depends on the dimensionless wave number  $b$  as follows

$$B = \frac{T_i}{T_e} \delta^2 b^2 \left[ \frac{\omega_{ce}^2}{\omega_{pe}^2} + \frac{1 - I_0(b) e^{-b}}{b} \right] \quad (6)$$

We note that for small  $b$ , the second term in the brackets behaves as  $1 - 3b/4$ .

As indicated above, for the two roots between  $\Omega = \pm 1$  being complex the value of  $B$  in eq.(5) must be below its critical value:

$$B < B_0 \equiv \frac{1}{4} \left( 1 + K^{1/3} \right)^3 \quad (7)$$

The strategy behind finding these two complex roots is very simple. First, we eliminate from consideration the remaining, always real roots that satisfy the condition  $|\Re\Omega| > 1$ , by writing

$$\Omega = p + iq$$

and requiring  $q \neq 0$ . This is a crucial requirement without which the relation between  $p$  and  $q$  in eq.(8) below would be meaningless. By separating the imaginary part of the l.h.s. of eq.(5) we obtain this relation as follows:

$$q^2 = \frac{\sqrt{1-p^2} (1-p)^{3/2} - \sqrt{K} (1+p)^{3/2}}{\sqrt{K} \sqrt{1-p} - \sqrt{1+p}} \quad (8)$$

Now, we need to derive an equation for  $p$ , by using the real part of eq.(5). After some straightforward algebra and elimination of  $q$  with the help of the above relation, we obtain

$$\sqrt{1-p^2} = \frac{2\sqrt{K}}{K+1-4Bp^2} \quad (9)$$

As may be seen, this is a cubic equation for  $p^2$  which is considerably easier to solve than the original eq.(5). Let us make the following transformation from  $p$  to  $\zeta$ :

$$p^2 = a(\zeta + 1) + 1, \quad \text{where} \quad a = \frac{K+1}{6B} - \frac{2}{3} \quad (10)$$

The equation for  $\zeta$  then reads

$$3\zeta - 4\zeta^3 = 1 + \frac{K}{B^2 a^3} \equiv Q \quad (11)$$

Depending on the value of its r.h.s.,  $Q$ , the last equation can be solved by one of the following three substitutions:

$$\zeta = \begin{cases} \sin \vartheta, & |Q| \leq 1 \\ \mp \cosh \phi, & Q \gtrless \pm 1 \end{cases} \quad (12)$$

In particular, for  $|Q| \leq 1$  one obtains

$$p^2 = 1 + \left( \frac{K+1}{6B} - \frac{2}{3} \right) \left\{ \sin \left[ \frac{1}{3} \sin^{-1} \left( 1 + \frac{6^3 K B}{(K+1-4B)^3} \right) + \frac{2\pi}{3} \right] + 1 \right\} \quad (13)$$

Actually, the domain of function  $Q(B)$  where  $|Q| \leq 1$  does not need to be addressed any further. Indeed, in this region either  $B < 0$  or  $B > B_0$ , Fig.3. The former case is clearly impossible, eq.(6). In the case  $B > B_0$ , as we know, all four roots of eq.(5) are real and, therefore, irrelevant to our analysis.

The two remaining possibilities with  $|Q| > 1$  in eq.(12) can be unified under one formula

$$p^2 = \frac{1}{3} + \frac{K+1}{6B} - \left| \frac{K+1-4B}{6B} \right| \cosh \left[ \frac{1}{3} \cosh^{-1} \left| 1 + \frac{6^3 K B}{(K+1-4B)^3} \right| \right] \quad (14)$$

which provides the real part of the frequencies of both damped and unstable modes. The imaginary parts (including the growth rate of the unstable mode) can be obtained from eq.(8). Observe that  $q^2(-p, 1/K) = q^2(p, K)$ . In fact, there are, only two roots with  $q \neq 0$ , not four, as one might infer from eqs.(14) and (8) with no recourse to the properties of the expression for  $q^2$ . This observation suggests the following choice of the sign of  $p$  when taking a square root from the expression on the r.h.s. of eq.(14). For  $K < 1$  we take the root  $p < 0$ , as to make  $q^2$  positive. For  $K > 1$  we then choose  $p > 0$ . After the correct sign of  $p$  is chosen, there are two complex conjugate roots with the imaginary parts given by eq.(8). The two remaining roots are always on the real  $\Omega$ - axis, since  $B, K > 0$ . These roots can easily be written in explicit form by factoring out the two complex roots from the full quartic equation, eq.(5).

Eqs.(14) and (8) thus provide the real and imaginary parts of the unstable mode in terms of  $K$  and  $B$ , eqs.(3,6). While  $K$  is straightforwardly related to the wave propagation angle with respect to the magnetic field, the parameter  $B$  depends on the main component of the wave vector,  $k_y \gg k_z$  in a more complicated fashion. We will thus use the dimensionless wave number  $b = |k_y| V_{Te} / \omega_{ce}$  instead of  $B$  in presenting the results for the frequency of the wave and for its growth rate in eqs.(14) and (8), respectively. For convenience, we rewrite  $B(b)$  using the following two parameters

$$\Delta = \frac{1}{4} \frac{T_i}{T_e} (\Omega_e - \Omega_i)^2, \quad \nu = \frac{\omega_{ce}^2}{\omega_{pe}^2}$$

So,

$$B(b) = b [\nu b + 1 - I_0(b) e^{-b}] \Delta$$

Furthermore, the normalization of  $\Omega$  contains  $k_y$  which was necessary to minimize the number of parameters in mathematical treatment of the dispersion eq.(5). Now we can return to the physical frequency  $\omega$  and growth rate  $\Im\omega$ , and express the results in terms of  $p$  and  $q$  as follows

$$\Re\omega = \frac{k_y}{2} [(V_{Ey} - V_{di})p + V_{Ey} + V_{di}] \quad (15)$$

$$\Im\omega = \frac{k_y}{2} (V_{Ey} - V_{di}) q \quad (16)$$

Here, the dimensionless frequency  $p$  and growth rate  $q$  are still given by eqs.(14) and (8). It is interesting to note that the real part of the frequency contains a convective contribution of combined drift speeds of electrons and ions,  $V_{di} + V_{Ey}$ . The second contribution is made by the relative ion-electron motion  $V_{Ey} - V_{di}$  which is solely responsible for the growth rate.

Shown in Figs.4 and 5 are the components of the frequency,  $bp$ , and growth rate,  $bq$ , as functions of  $K$  and  $b$ . These results characterize the dispersive and stability properties of LH waves and are key ingredients of the anomalous transport coefficients. The constant part of the phase velocity,  $V_{Ey} + V_{di}$  is subtracted from the surface plots. Now we can verify if the obtained solutions are consistent with simplifications made in deriving eq.(2) and how they are related to experiment conditions.

#### D. Verification and Discussion of the Solutions

While eq.(2) has a generic form in which it is broadly applied to many systems with counterstreaming plasmas and beams in plasmas, there are limitations, both general and specific to the case of colliding plasmas we consider here.

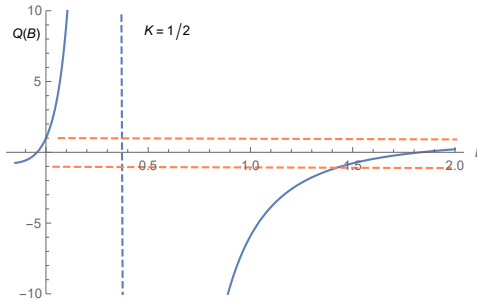


Figure 3. The function  $Q(B, K)$  on the r.h.s. of eq.(11) shown at  $K = 1/2$ . The vertical dashed line indicates the singularity at  $B = (K + 1)/4$ . The line  $Q = -1$  intersects  $Q(B)$  at  $B = B_0$ , so that the condition  $|Q(B)| < 1$  is met only for  $B > B_0$  where no complex roots are found.

First, eq.(2) describes local wave generation, not strictly applicable to inhomogeneous and finite plasmas. Indeed the colliding plasmas are interacting and mixing in a relatively thin layer, are inhomogeneous, and, in addition, can be subject to macroscopic instabilities, such as rippling of the plasma mixing layer [4]. Nevertheless, because of a very short scale of the LHDI instability ( $\sim \rho_e$ ), the requirement  $kL_s \gg 1$  is satisfied and the local approximation can be adopted ( $L_s$  is the width of the collision layer, sec.III C). With regard to the rippling effects, it indeed seems to be observed in some experiments within a small part of the shocked layer, though [16]. The field reconnection effects may play some role in this as the rippling is more pronounced on the anode side of the layer, where the electron current must be stronger, as they are accelerated by the reconnection electric field in  $y$ - direction. On the other hand, recent experiments specifically designed to study the reconnection layer in colliding flows do not show noticeable rippling of the reconnection layer [19].

Further constraints imposed on eq.(2) stem from the hydrodynamic treatments of ions. So, their velocity dispersion should be limited, even though their motion is randomized upon entering the shocked plasma layer. Therefore, we have to impose the condition  $\omega \gg kV_{Ti}$  which, in essence, means  $V_{Ey} \gg V_{Ti}$ . We will consider the electric field structure in the shocked plasma layer in detail further in the paper, but for the purpose of specifying the above restriction we can estimate  $V_{Ey} = cE_x/B \sim c\phi_s/L_s B$ , where  $\phi_s$  is the electrostatic potential built up in the shocked plasma layer. It can be estimated from the flow deceleration requirement,  $e\phi_s \sim m_i u^2$ , where  $u$  is the flow speed upstream from the shocked layer. Combining both inequalities, we obtain the following simple condition

$$\frac{\rho_e}{L_s} \ll 1 \ll \frac{\rho_i}{L_s} \quad (17)$$

where  $\rho_i$  is the ion Larmor radius and we have substituted the randomized ion velocity,  $V_{Ti} \sim u$ . Potentially problematic may be the right part of this condition. However, the experiment [16] indicates that the corona outflow speed  $u \sim 100$  km/s, while the magnetic field remains in the range of 10 kG. These numbers yield for the ion Larmor radius  $\rho_i \sim u/\omega_{ci} \sim 10^{-1} A/Z$  cm, where  $A$  and  $Z$  are the mass and charge numbers of the ion. Since the shocked layer in the experiment is shown to be significantly narrower than the gap between the wires,  $a = 2$  mm, the condition in eq.(17) holds up, at least for incompletely ionized ions with  $A \gg 1$ . The recent reconnection dedicated experiments [19] reach significantly higher magnetic fields but also much stronger ion heating is observed, so the above condition appears to be met as well. We also note here, that in the interest of light notation, we do not include mass and charge numbers  $A, Z$  of the ions in the dispersion equation. They can be easily restored by replacing  $m_i \rightarrow Am_i$  and  $e \rightarrow Ze$  in terms, corresponding to the ion contribution.

To conclude our discussion of the applicability of the results, we observe that the waves propagate in  $y$ - direction, which is favorable for the homogeneous plasma approximation. Besides, the phase velocity has a constant ( $k$ -independent) component  $V_{Ey} + V_{di}$  that remains finite even if the variable component  $\sim p$  becomes small for  $K \sim 1$ . Note that the signs of the both drift velocities  $V_{Ey}$  and  $V_{di}$  coincide as both the magnetic fields around each wire and the directional ion motion are associated with parallel currents. This makes the condition in eq.(17) easier to fulfil. Moreover, even when the real part of the frequency, associated with  $p$ -dependent contribution is small, the imaginary part of  $\omega$  becomes large at  $K \sim 1$ , thus reinforcing the condition in eq.(17). Note that the most unstable waves are those with  $K \sim 1$  (almost perpendicular to  $B$ ),  $k_z/k_y \sim \sqrt{m/M}$ . As  $p < 1$  (Figs.4-5), they propagate in the electron and ion drift direction (positive  $y$ - direction), according to eq.(15).

### III. MACROSCOPIC PROPERTIES OF COLLIDING FLOWS

In the preceding section, we obtained an exact formula for the growth rate of LH-drift instability occurring in the region where two concentric outflows from two exploding wires collide. They stream sideways from the collision center line between the wires at  $x = z = 0$ . The purpose of this section is to characterize the resulting flow pattern whose parameters enter the stability analysis of the preceding section.

#### A. The Overall Flow Configuration

The analysis in the previous section indicates that the electron  $\mathbf{E} \times \mathbf{B}$ -drift in the flow collision region powers a strong LHDI instability. The drift is supported by the electrostatic field  $E_x$  built up in the flow around the symmetry plane (magnetic zero). The  $\mathbf{E} \times \mathbf{B}$  drift is then in  $y$ - direction,  $V_{Ey} = cE_x/B$ . It is more important than electron and ion drifts associated with the external and reconnection field  $E_y$  for the following two reasons. First, the latter is narrowly concentrated in the magnetic null plane. This region is only  $\sqrt{\rho_e L}$ - wide, where  $L = B/(dB/dx)$  is the neutral layer characteristic scale which is obviously the same as the flow collision region. By contrast, the  $E_x$  field is

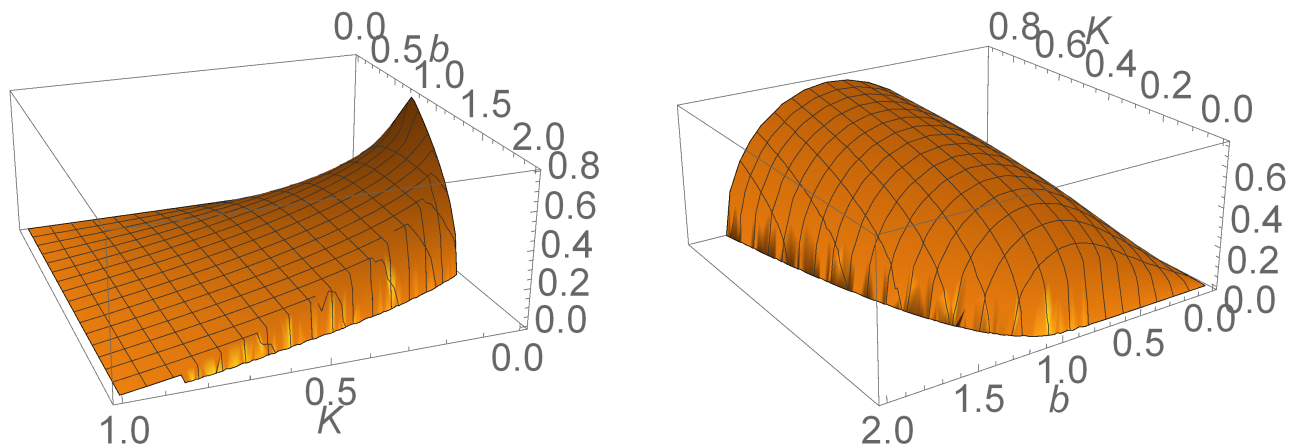


Figure 4. Left panel:  $bp$ , a dimensionless dependence of the real part of frequency  $\omega$ , as a function of  $b$  and  $K$ . Shown is the unstable region on the plane  $(b, K)$ , where  $\Im\omega > 0$ , eq.(15), for  $\Delta = 1$  and  $\nu = 0.2$ . Right panel:  $bq$ , the imaginary part of  $\omega$ , using the same normalization as  $bp$ .

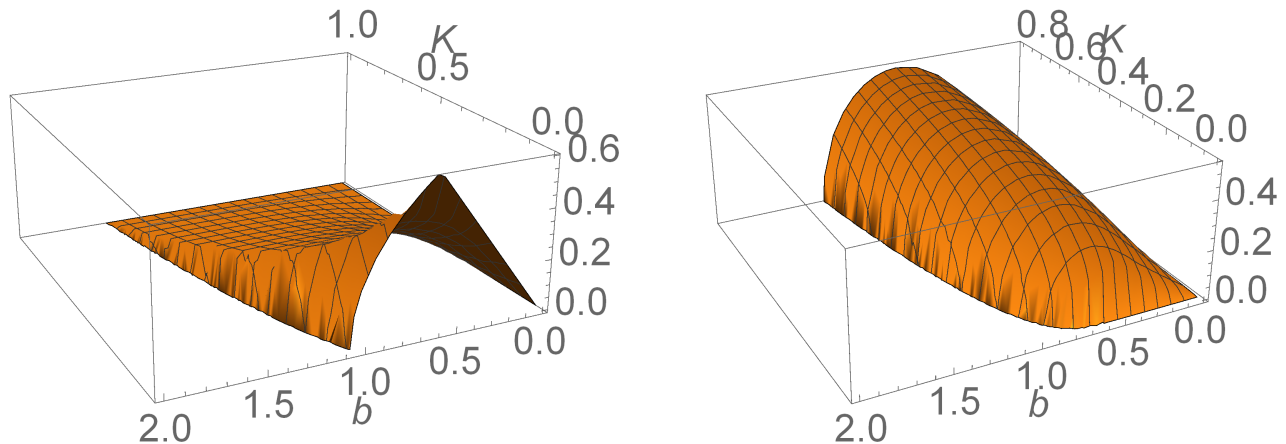


Figure 5. The same as Fig. but for  $\Delta = 2$ .

supported by the flow collision and associated charge separation caused by the inertial forces in the colliding flows. Second, the experimental information obtained from the explosive evaporation of specifically two wires [16] point to a rapid voltage collapse, thus indicating a short-circuiting of  $E_y$  field.

To get a grasp of the flow, it is useful to temporarily replace the two colliding flows, Fig.6, by one, that flows out concentrically from the point  $x = -a$  and collides with a reflecting wall placed at the symmetry plane at  $x = 0$ . A necessary disclaimer to make here is that an important and likely observable [16] rippling of the magnetic null surface is not captured by this simplified treatment. Apart from this limitation, and assuming a steady state with the conventional symmetry arguments, the two flow configurations are equivalent. If, in addition, the plasma inflow was strictly parallel to the  $x$ - axis rather than concentric, after having hit the wall, the flow could be described as a typical numerical setup to simulate the shock waves. Namely, upon a specular reflection off the wall, the reflected flow couples to the incident one and a shock wave forms[13]. Its structure and speed at which it propagates away from the wall will depend on the Mach number of the inflowing plasma. This parameter may be assumed to be larger than unity (so, the shock must form) but not strongly so, as the adiabatic cooling of the cylindrical flow scales as  $T \propto r^{1-\gamma}$ , where  $\gamma$  is the adiabatic index of the coronal phase. The cooling starts from about  $r \sim 10^{-3} - 10^{-2}$ cm and ends at  $r \sim a = 10^{-1}$ cm, e.g., in the experiment [16]. Although the flow is magnetized and the shock will be of a magnetosonic type, the plasma ram pressure typically exceeds the magnetic pressure by a significant factor ( $\sim 10$ ) [16], so we can consider an electrostatically, rather than magnetically, dominated ion-acoustic shock instead.

Regardless the shock type, its important aspect is a critical Mach number (at which it starts reflecting the upstream ions). Its exact value for the ion-acoustic shocks significantly depends on the electron distribution. For Boltzmannian electrons,  $M_{cr} \approx 1.6$  [15], while for adiabatically trapped electrons  $M_{cr} \approx 3.1$ , [6]. The choice between these two



models should be made depending on the macroscopic consequences of the LH instability. It is reasonable to expect that this instability will result in a strong electron heating and spatial diffusion, in particular.

From the above consideration the following picture emerges: two coronal flows, directed radially from the points  $x = \pm a$ , collide at  $x = 0$  and couple (presumably by a two-stream, Buneman instability). Then, they slow down and decline sideways along the  $z$ - axis from the flow stagnation line,  $x = z = 0$ . Note, that although we do not consider this initial two-stream instability here, it can be described by the same type of dispersion equation as eq.(5), studied in detail in Sec.II C. The forces that slow down and deflect the flow originate from an electrostatic potential  $\phi$  built up in response to the interaction of colliding flows and a pondermotive potential,  $\Phi$ . It is connected with the unstable oscillations, discussed in Sec.II C. In plasmas at equilibrium, the two potentials are usually related:  $\phi = -T_i\Phi/(T_i + T_e)$ . In the case under consideration, the ion inertial forces violate this simple balance. Evidently, the flow must remain supersonic far away from the stagnation point, since at large distances it becomes equivalent to a single wire outflow. So, the downstream subsonic flow must transit through the sonic point again while flowing out from the plane of the wires (in  $z$ - direction). Furthermore, two shocks are formed, as we show below, roughly parallel to the mid-plane and propagate into the respective flows, Fig.6. Technically, we can look for a steady state shock solution as long as the inflowing plasma can be considered stationary. We assume that this is the case and do not consider here the arrival of the wire core material that is expected at later times [16].

### B. Simplified Equation for the Flow

We will write the equations for colliding flows, using the following normalized variables. The flow velocity will be measured in the units of ion-sound velocity,  $C_s = \sqrt{T_e/M}$ , the potentials (both electrostatic and pondermotive,  $\phi$  and  $\Phi$ ) in units of  $T_e/e$ . The density is normalized to that of the corona,  $n_0$ , near the surface where it starts to rise due to the flow collision, but where the both potentials are still at zero values. This region is just upstream of the shocks, standing in the flows between the wires. Since this density changes along the  $z$ - coordinate we take its value at  $z = 0$  for the normalization purpose. Writing the Poisson equation below, we measure the lengths in the units of Debye length,  $\lambda_e = \sqrt{T_e/4\pi e^2 n_0}$ , while other equations are scale-invariant. For a stationary flow, they can be written in the following way

$$\frac{1}{2} (v_x^2 + v_z^2) + \phi + \frac{T_i}{T_e} \ln n_i = \frac{1}{2} w_0^2 = const \quad (18)$$

$$\frac{\partial v_x}{\partial z} - \frac{\partial v_z}{\partial x} = 0$$

$$\phi + \Phi - \ln n_e = 0 \quad (19)$$

$$\frac{\partial}{\partial x} n_i v_x + \frac{\partial}{\partial z} n_i v_z = 0 \quad (20)$$

$$\Delta\phi = e^{\phi+\Phi} - n_i \quad (21)$$

Several remarks about the above equations are in order here. First, we have replaced the equation of motion for the ions by the Bernoulli's integral in the first equation above, assuming that the flow remains irrotational (second equation) also after it passes the shock. An alternative, but in that regard equivalent, possibility is that for a relatively low-Mach

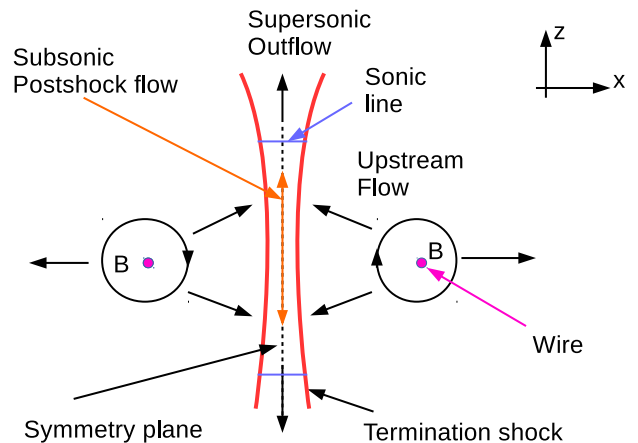


Figure 6. Colliding flows on  $x - z$  plane.

number flow the transition from the upstream to downstream region is smooth. In this case the last equation can be replaced by a simple quasi-neutrality condition,  $n_e = n_i$ . Given the quasi-homogeneous flow upstream of both shocks, that are relatively flat as we argue below, the curl-free condition,  $\partial v_x / \partial z - \partial v_z / \partial x = 0$ , is a plausible approximation [7]. It is essential for closing the system of the three equations that follow. The ponderomotive potential,  $\Phi$ , needs to be determined separately. We will calculate it in a future study based on the growth rate obtained in Sec.II C and on the overall flow structure addressed in this section.

As the quasineutrality condition is not yet implemented in the Poisson equation, the above equations capture the electrostatic shock transition. However, the ion density  $n_i$ , except for the vicinity of the shock transitions, is indeed very close to the electron density,  $n_e$  (quasineutrality condition), as already mentioned. The equation of motion for electrons is replaced by a simple balance condition between the ponderomotive, electrostatic and pressure forces. The balance results in a Boltzmannian distribution in the total potential  $\phi + \Phi$ , as may be seen from eq.(19). An alternative model for the electron distribution near the shock front assumes their adiabatic trapping in the shock potential [6]. In this case the critical Mach number beyond which the ions begin to reflect off the shock is about a factor two higher than in the case of Boltzmannian electron distribution, where  $M_{cr} \approx 1.6$ . These values have, however, been obtained for one-dimensional ion-acoustic shocks and can be used only as guide lines in the two-dimensional flow analysis.

To minimize the number of parameters in the above system of equations (only two of them remain,  $T_e/T_i$  and  $w_0$ ), we have chosen the Debye length,  $\lambda_D$ , for the space scale. This is a natural scale to describe the shock transition and it is too short for the rest of the flow. However, as we apply the quasi-neutrality condition (outside of the shock transition we can set  $\Delta\phi = 0$ ) the above system becomes scale-invariant, and we can use any other convenient scale, e.g., the distance between the wires,  $2a$ , etc. To conclude this introduction of the equations used in this section we note that some of the auxiliary notations from Sec.II will be reused here, which should not cause confusion.

The 2D-flow described by the above equations is depicted in Fig.6. The back-transitions to the supersonic flows, shown by the two ‘‘sonic lines,’’ logically follows from the equivalence of the double- and single-wire flows at large distances from the origin ( $r \gg a$ ), as we pointed out earlier. An equivalent single-wire coronal flow is presumed to be marginally supersonic, according to the corona parameters inferred from the experiments [16].

### C. Analysis of Colliding Flows

Referring to Fig.6 again, let us focus on the region enclosed by the two shocks and two sonic lines. We need to calculate the width  $2X_s(x)$  of the post shock region between the shocks at  $|x| < X_s(z)$ , as it determines the scale of the macroscopic electric field  $E_x$  that, in turn, sets the growth rate of the LHDI. This quantity needs to be related to the flow Mach number  $w_0 = \sqrt{v_x^2 + v_z^2}$  (the velocities are already measured in units of  $C_s$ ) and the jump of electrostatic potential,  $\phi_s(z)$ , at the termination shocks. This jump is similar to the maximum potential of the conventional ion-acoustic soliton with a trailing oscillatory structure [12, 15]. There are several important distinctions, though.

First, we are dealing with a two-dimensional shock with gradually changing flow angle from the normal incidence at  $z = 0$  to the increasingly oblique shock geometry at  $z \gtrsim a$ . Besides, the shock weakens with  $z$  to merge into the radial supersonic outflow at large  $z \gg a$ , beyond the outflow sonic line. Since the shock is generally oblique, in applying the shock jump conditions we will allow only the normal velocity component to jump while keeping the tangential one continuous across the shock surface. Second, as the upstream flow cross the shock at a variable distance from the centers of the outflows located at  $x = \pm a$ , the upstream shock conditions also change. Finally, the shock electrostatic potential, while possibly oscillating in a narrow region (a few  $\lambda_{De}$ ) behind the shock transition (as in the ion-acoustic

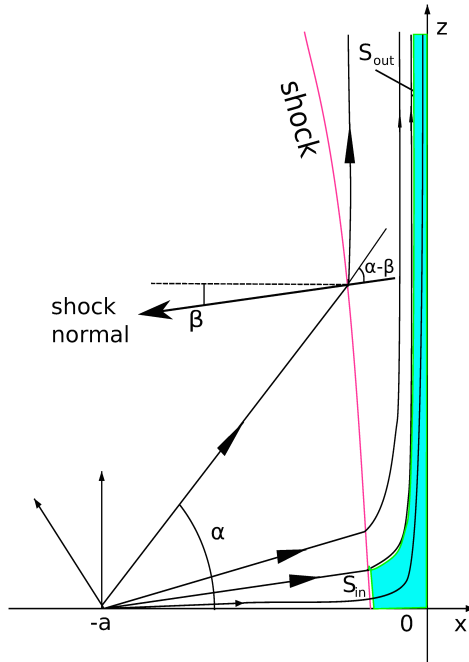


Figure 7. Plasma flow past the right angle at  $x = z = 0$ , that is equivalent to the colliding outflows under two-way symmetry:  $x \rightarrow -x, z \rightarrow -z$ .

shocks with the ion reflection, studied in [10]), on average it must gradually increase towards the mid-plane. This is a symmetry requirement, since ions must progressively deviate from the center-line of the flow downstream ( $z = 0$ ). For the same reason, the flow must stagnate at the point  $x = z = 0$ . We will discuss this aspect of the shock in more detail in Sec.III D.

Assuming the quasineutrality condition in the shocked part of the flow, from eqs.(18-21) we obtain the following relation between the maximum electrostatic potential,  $\phi_{\max}$ , and the Mach number,  $w_0$ :

$$\phi_{\max} = \frac{\frac{w_0^2}{2} - \frac{T_i}{T_e} \Phi_0}{1 + \frac{T_i}{T_e}} \quad (22)$$

Here  $\phi_{\max}$  and  $\Phi_0$  relate to the point  $x = z = 0$ . It is seen that the micro-scale flow instability, studied in Sec.II C and entering the flow potential through the pondermotive potential  $\Phi$ , may play a key role in mediating the electrostatic shock and shaping the flow. This effect is expected to be more pronounced in strong shocks where the ion velocity randomization upon shock crossing (higher  $T_i$ ) strongly dominates the electron shock thermalization. At the same time, the electron heating should also result from the lower-hybrid instability and will, on the contrary, diminish the role of the pondermotive pressure.

Our purpose here, however, is to understand the general characteristics of the flow and estimate the shock stand-off distance, that is the width of the shocked plasma layer, as a function of  $z$ . These characteristics of the flow will provide information about the electrostatic potential, that includes the shock jump condition and its post shock growth up to its maximum at the flow stagnation point. The potential profile is key in calculating the flow micro-instabilities, studied in Sec.II. It is clear that this potential slows down and compresses the colliding flows as the internal and pondermotive pressures also do. However, the maximum flow compression (downstream to upstream density ratio) is limited by a factor depending on the polytrope index.

$$n_2/n_1 = (\gamma + 1) / (\gamma - 1 + 2/w_0^2),$$

where  $w_0$  is the Mach number of the flow ahead of the shock. Note, however, that due to radiation and ionization effects, especially in dense plasmas, the polytrope index may be significantly lowered compared to the familiar mono-atomic gas  $\gamma = 5/3$ , e.g. down to  $\gamma \approx 1.2$  [5]. Indeed, according to the observations [16], the layer of compressed plasma between the wires is rather thin. We therefore consider the electrostatic potential to be the primary flow decelerator. As we will see below, in this case the system given by eqs.(18-21) is equivalent to the set of gasdynamic equations with the adiabatic index  $\gamma = 1$ .

That the electrostatic potential is capable of compressing a cold ion flow ( $T_i \ll T_e$ ) significantly stronger than the adiabatic compression, can be illustrated by considering a simple ‘‘water bag’’ model. According to this model, the ions are distributed in the normal to the shock speed  $v$  in the following way  $f_i(v) = \eta(v - v_1) \eta(v_2 - v)$ . Here  $\eta$  is the Heaviside unit function and  $v_2 > v_1$ . By virtue of Liouville’s theorem and particle energy conservation, after passing over a potential jump of the height  $\phi$ , the ion distribution becomes  $f_{id}(v) = \eta(v - \sqrt{v_1^2 - 2\phi}) \eta(\sqrt{v_2^2 - 2\phi} - v)$ . So, the flow compression ratio can be written as:

$$\frac{\sqrt{v_2^2 - 2\phi} - \sqrt{v_1^2 - 2\phi}}{v_2 - v_1}$$

The flow compression reaches its maximum when the slowest particles with  $v = v_1$  begin to reflect, that is for  $\phi = v_1^2/2$ , we can write

$$\sqrt{\frac{v_2 + v_1}{v_2 - v_1}} \sim \sqrt{V_i/V_{Ti}}$$

where  $V_i$  and  $V_{Ti}$  denote the ion bulk and thermal velocities, respectively. This compression may indeed considerably exceed that of the conventional shock adiabat for a cold and fast ion flow thus being more consistent with the observations [16]. To further simplify the derivation we neglect the ion pressure contribution in Bernoulli eq.(18), by assuming that the balance in it is dominated by electrostatic and inertial forces on the flow. Neglecting also the deviation from quasineutrality in the post shock region, we rewrite the system given by eqs.(18-21) as follows

$$v_x^2 + v_z^2 + 2\phi = w_0^2 = const \quad (23)$$

$$\frac{\partial v_z}{\partial x} - \frac{\partial v_x}{\partial z} = 0$$

$$\frac{\partial}{\partial x} v_x e^\phi + \frac{\partial}{\partial z} v_z e^\phi = 0 \quad (24)$$

In view of the  $n_e = n_i$  approximation made here, these equations do not describe the shock transition and will only be applied to the flow in the shocked plasma between the two termination shocks. In the conventional gasdynamics, a termination shock forms where the ram pressure of the outflow is equilibrated by the pressure of the ambient medium. In the case of colliding flows considered here the pressure of shocked plasma between the two shocks plays the role of the pressure of the ambient medium. In our model, however, the electrostatic potential appears to be a better mediator between the counter-streaming flows. Most of its rise in the stagnating flow occurs immediately at the shock transition. The cross shock potential can be obtained from the local treatment in a one-dimensional shock approximation. Now we focus on the two-dimensional post-shock flow.

Introducing the flow potential  $\chi$  by

$$v_x = \partial_x \chi, \quad v_z = \partial_z \chi, \quad (25)$$

we rewrite eqs.(23-24) in the following form

$$|\nabla \chi|^2 + 2\phi = w_0^2 \quad (26)$$

$$\Delta \chi + \nabla \chi \cdot \nabla \phi = 0, \quad (27)$$

where  $\nabla = (\partial_x, \partial_z)$ . By the symmetry of the flow, it is sufficient to consider the flow in any quadrant of the  $x - z$  plane and the adjacent part of the respective shock, Fig.7. The flow is then past the interior of the  $90^\circ$ - angle, e.g. from the positive  $x$  direction at  $x < 0$ ,  $z \approx 0$  turning to the positive  $z$ - direction at  $z > 0$ ,  $x \approx 0$ . The boundary conditions at the walls of the corner are dictated by the symmetry requirements at  $x = 0$ :  $\partial_x \chi = 0$ ,  $\partial_x \phi = 0$ , and similar conditions at  $z = 0$ :  $\partial_z \chi = 0$ ,  $\partial_z \phi = 0$ . Substituting  $\phi$  from eq.(26) into eq.(27) one can obtain one equation for the flow potential

$$\Delta \chi = \frac{1}{2} \nabla \chi \cdot \nabla |\nabla \chi|^2 \quad (28)$$

The above system or, equivalently, the system given by eqs.(23-24) can be linearised by transforming it to a hodograph plane, e.g. [8], on which dependent and independent pairs of variables interchange. The problem is, however, in the boundary conditions at the shock whose position is unknown beforehand and should be determined self-consistently with the flow past the shock. This makes the application of hodograph method rather problematic. We therefore begin with an approximate analysis of the system given by eqs.(26-27).

Referring to Fig.7, let us consider first the flow near the corner  $x = z = 0$ . As this is the stagnation point, we can neglect nonlinear velocity terms, to the first order of approximation. Specifically, the first term in eq.(27) is of the order of  $v/L_s$  while the second term is  $v^2 \ll 1$  times smaller. Here  $L_s$ , stands for the distance between the shock and the flow stagnation point, while the function  $X_s(z)$ , introduced earlier, is related to  $L_s$  by  $L_s = X_s(0)$ . The flow potential near the stagnation point can then be approximated by a harmonic function,  $\Delta \chi = 0$ . Given the boundary conditions, we can write the solution of the Laplace equation as

$$\chi \approx \frac{U_0}{2L_s} (z^2 - x^2) \quad (29)$$

Here the post shock velocity  $U_0 \equiv v_x(-L_s, 0)$  is taken at the mid-plane  $z = 0$ . It will be specified later using the shock jump conditions. The electrostatic potential near the stagnation point can now be obtained immediately from eq.(26):

$$\phi \approx \frac{w_0^2}{2} - \frac{U_0^2}{2L_s^2} (x^2 + z^2) \quad (30)$$

It follows that the flow changes its direction from predominantly horizontal at  $z < |x|$  to vertical at  $z > |x|$ , deflected by the potential hump in eq.(30).

To gain more insight into the shock geometry, let us integrate the continuity eq.(24) over a narrow region inside the flow (filled region in Fig.7). This region is confined by the two adjacent streamlines and the two lines transversal to the flow that the flow crosses when entering and exiting the region. Let the first transversal has a length  $S_{in}$ , being a part of the shock surface. The second transversal, of the length  $S_{out}$ , is far away from the stagnation point, where the flow accelerates to its preshock speed, that is beyond the sonic line. The contributions to the integral from the two stream lines vanish, while the contributions from the lines  $S_{in}$  and  $S_{out}$  remain. So, we obtain

$$S_{in} e^{\phi_s} \sqrt{w_0^2 - 2\phi_s} = S_{out} w_0$$

For shocks near criticality, where the cross shock potential  $\phi_s$  is about to reflect the inflowing ions  $w_0^2 \approx 2\phi_s$ , we arrive at a strong inequality  $S_{in} \gg S_{out}$ . We have taken into account that the exponential factor is typically not very large. For example, the critical Mach number of an ion-acoustic shock with Boltzmannian electrons is  $w_{cr} \approx 1.6$ , as we mentioned earlier. For the adiabatically trapped electrons, though, this quantity is higher,  $w_{cr} \approx 3.1$ . The former model is, however, a better choice for the case considered, as reasonably frequent electron-ion collisions should maintain the local Maxwellian.

From the above relation we see that the flow tubes become asymptotically narrower by a factor  $\sim (1 - 2\phi_s/w_0^2)^{1/2} \ll 1$  upon passing the corner at the stagnation point  $x = z = 0$ . For an estimate, we can assume the cross-section of the net inflow  $S_{in}$  to be  $S_{in} \lesssim a$ . Indeed, for larger  $S_{in}$  the flow incidence angle with respect to the shock normal becomes large enough for particle reflection and these particles do not enter the post-shock space. Thus, we obtain for the total width of the outflow  $S_{out} \lesssim (1 - 2\phi_s/w_0^2)^{1/2} a \ll a$ , with an implication that the shock region width  $L_s \ll a$ , which is consistent with the experiments [16].

#### D. Shock geometry and cross-shock potential

We have found the shocked plasma in colliding flows to form a thin shell between two shocks terminating each flow. Now we wish to understand the shape of this shell, which requires the knowledge of the flow velocity between the shocks and the distribution of electrostatic potential along the shock surface. Under the symmetry conditions and constraints concerning the shocked plasma flow, that we discussed and accepted earlier, we can replace this flow by an equivalent one. This latter flow is between one shock and the two rigid walls making the right angle, as depicted in Fig.7.

The flow velocity on the downstream side of the shock surface can be expressed through the shock jump conditions, Fig.7:

$$v_\tau = w_0 \sin(\alpha - \beta) \quad (31)$$

$$v_n = \sqrt{w_0^2 \cos^2(\alpha - \beta) - 2\phi_s} \quad (32)$$

They constitute the continuity of the tangential component of the flow velocity and the jump of its normal component due to the cross-shock potential  $\phi_s$ , under the conservation of particle energy during the shock crossing. As in the previous subsection,  $w_0$  denotes the flow velocity ahead of the shock, while  $v_n$  refers to the normal velocity component downstream from the shock surface. The angles  $\alpha(z)$  and  $\beta(z)$  refer to the flow angle to the  $x$ - axis ahead of the shock and the shock angle to  $z$ - axis, respectively. These angles are related to the distance between the shocks separation,  $2X_s(z)$ , by

$$\tan \alpha(z) = \frac{z}{a - X_s(z)}$$

$$\tan \beta(z) = \frac{dX_s}{dz}$$

where  $X_s(z) > 0$  is the shock distance from the mid-plane  $x = 0$ , Fig.7. We have already discussed the two remaining boundary conditions at the “walls”  $x = 0$  and  $z = 0$ .

At the distances  $z \gg L_s$  from the flow base line  $z = 0$ , the shocked flow is directed nearly vertically. This is dictated by the alignment of the stream lines coming from the bottom parts of the shock along the  $z$ - axis. The sharp turn of the flow from  $x$  aligned to  $z$ - aligned can be described by the flow structure and electrostatic potentials already given in eqs.(29) and (30). As we already argued, for shocks with sufficiently high Mach numbers, when the ions are about to reflect, they move very slowly in the shock normal direction. Therefore, the change of the flow direction will occur in a narrow layer near the shock front.

To begin with a preliminary sense of how the shock potential is distributed along the shock surface, we make the following simplification. Instead of resolving this narrow layer and matching the solution to the nearly vertical flow between the shocks, we can collapse this region and require that the flow becomes vertical immediately after the shock crossing. That is, we impose the condition  $v_x(-X(z), z) = 0$  which translates into the following relation

$$\cos \beta \sqrt{\cos^2(\alpha - \beta) - 2\phi_s(z)/w_0^2} - \sin(\alpha - \beta) \sin \beta = 0 \quad (33)$$

The  $z$ - component of the flow velocity can then be written as follows

$$v_z = w_0 \frac{\sin(\alpha - \beta)}{\cos \beta}$$

One can also obtain a very simple expression for the  $\phi_s(z)$  dependence where  $z$  is sufficiently large, so that the flow incidence angle is not small,  $\alpha \gg \beta$ . As we argued, the shock surface must be well aligned with the vertical axis, so we may set  $\beta \approx 0$ . Under these conditions, from eq.(33) we have

$$\phi_s(z) = \frac{1}{2} \frac{w_0^2}{1 + z^2/a^2} \quad (34)$$

The electrostatic potential decreases with growing  $z$  along the shock front as to keep its strength close to criticality. The upstream plasma impinging on the shock surface thus loses its horizontal velocity component or even reflects from the shock at sufficiently large  $z$ , when the incidence angle  $\alpha$  is not too small.

### E. Hodograph Equations

Now that we have a better grasp of the flow between the shocks, we shall attempt at the analysis of its properties on a more accurate basis. For this purpose, we shall map the nonlinear eqs.(23-24), describing a plane-parallel flow on the  $x, z$  -plane to the so-called hodograph plane. In the new form, the equations will be linear. Meanwhile, the original equations represent a special case of the gas of  $\gamma = 1$  adiabat (or isothermal flow, cf. eqs. [23] and [24]), since the quasi-neutrality condition and the Boltzmann distribution for electrons require the electrostatic potential to play the role of the specific enthalpy of the gas in the following form:  $\phi = \ln \rho$ . This does not make the hodograph transform derivation any different from the conventional gas-dynamic case with  $\gamma > 1$ . We therefore provide only the key steps of this derivation in Appendix A. As usual, the main problem in applying the hodograph method is in the boundary conditions of the flow.

We will study a specific part of the flow that is confined by the shock surface and two axes of symmetry ( $x = 0, z > 0$  and  $z = 0, x < 0$ ), as shown in Fig.7. The fourth line, that closes the boundary of the flow under consideration, is drawn somewhat arbitrarily in the outflow region where  $z \gtrsim a$ . The flow is accelerated to transonic speeds in this region,  $v_z \lesssim C_s$  ( $v_z \lesssim 1$  in dimensionless variables that we use) while the  $v_x$  component becomes close to zero, as discussed in the preceding subsection. We introduce this latter boundary in the flow because we are not concerned here with the transition back to the supersonic regime that occurs far away from the flow stagnation point. To proceed on the hodograph derivation, in addition to the flow potential  $\chi$  used in the previous subsection, we introduce a stream function  $\psi$  in a usual way,

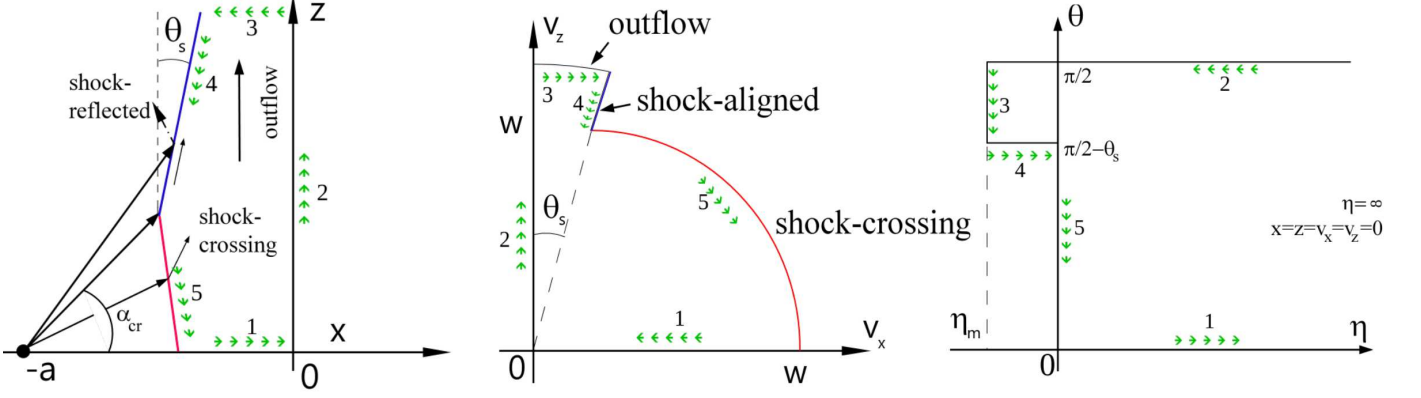


Figure 8. Hodograph transform: physical flow plane  $x, z$  (left panel);  $v_x, v_z$  plane (middle);  $\eta, \vartheta$  plane (right panel). The solid lines with arrows on the left panel schematically show the streamlines (see also Fig.7). The green arrows indicate the direction on the contour consisting of the segments 1-5 (see text).

$$\rho v_x = \frac{\partial \psi}{\partial z}, \quad \rho v_z = -\frac{\partial \psi}{\partial x} \quad (35)$$

Transforming from the  $x, z$  dependent variables to  $v_x, v_z$ , we use polar coordinates on the flow velocity plane adhering to the traditional hodograph notations  $q, \vartheta$  for them:

$$v_x = q \cos \vartheta, \quad v_z = q \sin \vartheta \quad (36)$$

The hodograph equations take then the following (Chaplygin) form, Appendix A:

$$\frac{\partial \chi}{\partial q} = \frac{q^2 - 1}{\rho q} \frac{\partial \psi}{\partial \vartheta} \quad (37)$$

$$\frac{\partial \psi}{\partial q} = \frac{\rho}{q} \frac{\partial \chi}{\partial \vartheta} \quad (38)$$

where, in accordance with eqs.(23,24)

$$\rho = \rho_0 e^{-q^2/2}, \quad \rho_0 = e^{w_0^2/2} \quad (39)$$

Again, we assume for simplicity that the plasma enters the shock with constant density (we normalized it to unity) and constant supersonic velocity  $w_0 > 1$ . In fact, this is not quite true and even though the constant velocity assumption is plausible (as is approximately the case in various supersonic outflows), the density is inversely proportional with the distance from the source at  $x = -a$ , just to conserve the flux, Fig.7. However, the most important part of the flow is at relatively low values of  $z \lesssim a$  since this is the region where the electric field drives the drift in  $y$ - direction and thus the lower-hybrid instability. Therefore, we may ignore the foreshock variations in the flow in view of much stronger changes in velocity and density occurring upon crossing the shock.

Formally, Chaplygin eqs.(37-38) are equivalent to the original system given by eqs.(23-24). Their two big advantages over the original system are that they are linear and the variables  $q, \vartheta$  are separable. As we mentioned earlier, the price of these simplifications is in the boundary conditions, since they must be formulated in terms of the flow velocity components as new independent variables, rather than fixed geometrical boundaries. At the same time, the specificity of our problem is that two of the boundaries are not known regardless of the form of governing equations in use.

These are the shock surface function,  $x = X_s(z)$  and the position of the sonic line. The latter, though, is of a lesser concern for this study.

These difficulties notwithstanding, our task can be simplified because the large part of the flow is strongly decelerated upon passing through the shock wave but not yet accelerated to the supersonic velocities ( $q > 1$ ), while proceeding in  $z$  direction. Therefore, we can consider the case of  $q < 1$  and observe some cancellations of the  $q$ -dependencies in coefficients of eqs.(37-38) for  $q \ll 1$ . These cancellations allow us to evaluate the Chaplygin equations to a system with constant coefficients, accurate to the order  $q^4$ . Indeed, to this accuracy we can rewrite eqs.(37-38) as follows

$$\frac{\partial \chi}{\partial q} \approx -\frac{1}{\rho_0 q} e^{-q^2/2} \frac{\partial \psi}{\partial \vartheta} \quad (40)$$

$$\frac{\partial \psi}{\partial q} = \frac{\rho_0}{q} e^{-q^2/2} \frac{\partial \chi}{\partial \vartheta} \quad (41)$$

This form of equations immediately suggests yet another change of variables

$$\eta = \int_q^w \frac{dq}{q} e^{-q^2/2}, \quad \Psi = \psi/\rho_0 \quad (42)$$

The variable  $\eta$  runs from its minimum value,  $\eta_m < 0$  (where the flow accelerates in  $z$ - direction to some maximum speed  $q_{max} > w$ , where  $z \gg a$ ) to infinity (flow stagnation point,  $q \rightarrow 0$ ). In these new variables the above equations constitute the familiar Cauchy-Riemann relations for  $\chi$  and  $\Psi$ :

$$\frac{\partial \chi}{\partial \eta} = -\frac{\partial \Psi}{\partial \vartheta}, \quad \frac{\partial \Psi}{\partial \eta} = \frac{\partial \chi}{\partial \vartheta}$$

Therefore, we can apply powerful tools of complex analysis to our further derivation of the analytic form of the flow, in a close similarity to the analyses of the special types of planar flows that are both irrotational and incompressible. Note, however, that being arguably irrotational our flow is highly compressible in physical variables. It is only the Chaplygin form, combined with the above change of variables, that makes the flow to appear incompressible in the new variables.

From this point on, we follow the standard methods of complex analysis and introduce a complex flow potential

$$\Lambda = \chi + i\Psi$$

defined on a complex plane

$$\sigma = \eta + i\vartheta$$

According to the above Cauchy-Riemann relations,  $\Lambda$  is an analytic function of  $\sigma$ , and its imaginary and real parts are harmonic functions

$$\Delta \chi = \Delta \Psi = 0, \quad \text{where} \quad \Delta \equiv \frac{\partial^2}{\partial \eta^2} + \frac{\partial^2}{\partial \vartheta^2} \quad (43)$$

Thus, our task is indeed significantly simplified and can be formulated now as the following Dirichlet problem: find an analytic function  $\Lambda$  in some region on the plane  $\sigma$  taking specific value at its boundary. We therefore need to define this boundary which we do in two steps. First, we map the flow region in  $x, z$  variables to that in  $v_x, v_z$  variables. These regions are shown in the left and middle panels of Fig.8.

To proceed, we break down the boundary of the part of the original physical flow under consideration in the five segments numbered from one to five in Fig.8. The segment 1 starts from the shock surface, going along the symmetry axis  $z = 0$  where the flow decelerates to reach the stagnation point at  $x = z = 0$ . The flow turns sharply by ninety degrees at this point. So, the segment 2 of the flow boundary goes along another symmetry axis, the  $z-$  axis. In reality, the flow continues to infinity along it, gradually increasing its speed, but we do not follow it beyond some velocity,  $v = q_m \lesssim 1$ , as we pointed out earlier. This rather technical condition allows for the subsonic approximation throughout the flow region. We therefore draw the segment 3 connecting  $z-$  axis with the shock surface along the line



with the constant  $q = q_m$ . The remaining segments 4 and 5 go along the shock surface. They are different in that the upstream ions cross the segment 5 and get reflected from segment 4, because of the insufficient velocity component normal to the shock to pass above the shock potential. This distinction is not easy to make beforehand, as the shock potential decreases with  $z$ , Sec.III D. Moreover, the particle incidence angle increases, thus showing an opposite trends with regard to the shock reflectivity. The flow is different from conventional hydrodynamic flows primarily because it allows for a multi-stream state upstream owing to particle reflection. On the downstream side of the segment 4, there is no plasma inflowing across the shock and the flow is purely tangential for the incidence angles  $\alpha > \alpha_{cr}$ , Fig.8.

Turning to the Dirichlet boundary conditions for the stream function  $\Psi$ , it must remain constant on those segments of the boundary where the flow is tangential. These are the segments 1,2, and 4. Obviously, the stream function value on the segments 1 and 2 are equal and we can set them to be zero,  $\Psi_1 = \Psi_2 = 0$ . Let the respective constant value on the segment 4 be  $\Psi_4 \neq 0$ . The difference between these two values of the stream function equals to the net mass flux starting from the segments 5 (inflow) and ending at segment 3 (outflow), according to the definition of  $\Psi$ , given in eq.(35). Since this is the same flux emitted from the wire into the angle  $\alpha_{cr}$ , we find

$$\Psi_4 = \frac{\alpha_{cr}}{2\pi} S \quad (44)$$

where we have denoted the mass flux per unit length of each wire by  $S$ . In the next subsection we consider the Dirichlet problem including its boundary conditions in more detail.

### F. Dirichlet Problem for the Stream Function and its Solution

The above-discussed boundary conditions relate to the physical plane of the flow, i.e.,  $x, z$ - plane. The equations in these variables are strongly nonlinear and difficult to solve, as discussed in Sec.III C. By contrast, the ‘‘solvable’’ version of those equations given by eq.(43) is defined on the hodograph plane  $\eta, \vartheta$ . Recall that we have transformed to these variables in two steps, Fig.8. First, we mapped  $x, z$ - plane to  $v_x, v_z$  and then to  $\eta, \vartheta$ . The new boundary conditions for the Dirichlet problem merit more attention. Let us start with considering a counter-clockwise contour formed by the segments 1-5 on the physical plane  $x, z$ . The image of this contour on the  $v_x, v_z$ -plane is depicted in the middle panel of Fig.8. Next, we give a complete formulation of the Dirichlet problem and describe the transformation of the above contour to the  $\eta, \vartheta$  plane, shown in the right panel of Fig.8.

In the new variables  $\eta, \vartheta$  the Dirichlet problem for  $\Psi(\eta, \vartheta)$  can be formulated in the following way: find a harmonic function  $\Psi$ ,

$$\frac{\partial^2 \Psi}{\partial \eta^2} + \frac{\partial^2 \Psi}{\partial \vartheta^2} = 0, \quad (45)$$

inside a boundary shown in the right panel of Fig.8 that takes the following values on this boundary:

1.  $\Psi = 0$  on segments 1 and 2,
2.  $\Psi = \Psi_3(\vartheta)$  on segment 3
3.  $\Psi = \Psi_4 = \text{const}$  on segment 4
4.  $\Psi = \Psi_5(\vartheta)$  on segment 5,

where the constant value  $\Psi_4$  is given by eq.(44). The function  $\Psi_5(\vartheta)$  monotonically increases from 0 to  $\Psi_4$  in the interval  $0 \leq \vartheta \leq \pi/2 - \vartheta_s$  and the function  $\Psi_3(\vartheta)$  monotonically decreases from  $\Psi_4$  to 0, in the interval  $\pi/2 - \vartheta_s < \vartheta \leq \pi/2$ .

As we already mentioned, it is the boundary conditions that make the Dirichlet problem difficult to solve, not the eq.(45). Therefore, the common strategy for solving such problems is in mapping the problem domain to a simpler one, using a conformal map to a new complex variable  $\zeta$ , that is  $\eta + i\vartheta = \sigma \rightarrow \zeta$ . As the map is conformal, it does not change the Laplace equation for  $\Psi$  that remains analytic also in the new variables. The semi-infinite domain in the  $\eta, \sigma$ - plane shown on the right panel of Fig.8 can be viewed as either a hexagon with two right angles at  $\eta = \infty$ ,  $\sigma = 0, \pi$ , or a pentagon with just one zero angle at  $\eta = \infty$ . We wish to map the region confined by the segments 1-5 on the  $\sigma$ - plane to the upper half of  $\zeta$ - plane, so the boundary on the  $\sigma$ - plane must be mapped to the real axis of the  $\zeta$ - plane. This map can most efficiently be built by using the Schwartz-Christoffel integral. From its perspective, the domain on the  $\sigma$ - plane is to be regarded as a pentagon with one zero angle at the infinity,  $\eta = \infty$ , rather than

a hexagon also mentioned above. We lay aside this latter interpretation of the semi-infinite domain until Sec.III G, where we consider a simplified flow example.

Here, we establish the correspondence between the five points on the real axis of the new  $\zeta$ - plane  $\zeta_3 < \zeta_2 < \zeta_1 < 0, 1$ , and the angles of the pentagon on  $\sigma$ - plane. We will distinguish, however, between the points  $\eta = \infty, \vartheta = 0, i\pi$  on the  $\sigma$ - plane by ascribing different arguments to the linear function  $1 - \zeta$ , involved in the Schwartz-Christoffel integral. The correspondence is as follows:

1.  $\sigma = 0 \rightarrow \zeta = 0$
2.  $\sigma = i(\pi/2 - \vartheta_s) \rightarrow \zeta = \zeta_1$
3.  $\sigma = \eta_m + i(\pi/2 - \vartheta_s) \rightarrow \zeta = \zeta_2$
4.  $\sigma = \eta_m + i\pi/2 \rightarrow \zeta = \zeta_3$
5.  $\sigma = \infty + i0 \rightarrow \zeta = 1, \arg(\zeta - 1) = \pi$
6.  $\sigma = \infty + i\pi/2 \rightarrow \zeta = 1, \arg(\zeta - 1) = 0$

Then, the Schwartz-Christoffel map of the real axis  $\zeta$  to the flow region on the  $\sigma$  plane can be written as follows:

$$\sigma = \Theta \int_0^\zeta \sqrt{\frac{\zeta - \zeta_1}{(\zeta - \zeta_2)(\zeta - \zeta_3)(1 - \zeta)\sqrt{\zeta}}} d\zeta \quad (46)$$

Some details of the derivation of this result can be found in Appendix B. Now writing the new variable  $\zeta$  as  $\zeta = \zeta' + i\zeta''$ , the solution of the Dirichlet problem for the stream function can be represented in the form of Poisson integral

$$\Psi(\zeta', \zeta'') = \frac{\zeta''}{\pi} \int_{-\infty}^{\infty} \frac{\Psi(t, 0) dt}{(t - \zeta')^2 + \zeta''^2} \quad (47)$$

The earlier formulated boundary conditions for the Dirichlet problem require the function  $\Psi(\zeta', 0)$  under the integral to be defined as follows

$$\Psi(\zeta', 0) = \begin{cases} 0, & -\infty < \zeta' \leq \zeta_3 \\ \Psi_3(\zeta'), & \zeta_3 < \zeta' < \zeta_2 \\ \Psi_4 = const, & \zeta_2 \leq \zeta' \leq \zeta_1 \\ \Psi_5(\zeta'), & \zeta_1 < \zeta' < 0 \\ 0, & 0 \leq \zeta' < \infty \end{cases} \quad (48)$$

where  $\Psi_4 = const$  is given by eq.(44). The boundary functions  $\Psi_5(\zeta)$  can be defined by considering the flow in front of the shock. Using the cylindrical coordinates for velocity, by the definition of the stream function, eq.(35), we have

$$r\rho w_0 = \frac{\partial \Psi}{\partial \alpha} = \frac{S}{2\pi},$$

(cf. eq.[44]), where  $r$  is the distance to the wire; according to the notations of Sec. 13, we denote the angle made by the flow velocity with the  $x$ - axis upstream by  $\alpha$ . Here  $w_0$  is the radial velocity of the flow coming from the wire center at  $x = -a$ . Therefore, ahead of the shock the stream function changes linearly with  $\alpha$

$$\Psi = \frac{\alpha}{2\pi} S \quad (49)$$

Now we need to relate the angle  $\alpha$  upstream with that of downstream of the shock,  $\vartheta$ :

$$\cos \vartheta = \frac{v_n \cos \beta - v_\tau \sin \beta}{\sqrt{w_0^2 - 2\phi_s}}$$

where  $v_n$  and  $v_\tau$  are the normal and tangential to the local shock normal components of the flow velocity downstream,  $\beta$  is the shock inclination angle, and  $\phi_s$  is the cross-shock potential (see eqs.[31-32]). Note that in our construction of the hodograph plane in Sec.III E, the shock potential  $\phi_s \approx \text{const}$  for  $\alpha < \alpha_{cr}$ , Fig.8. At this critical angle the incoming ions begin to reflect off the shock. If we were to relax this simplifying condition, the flow velocity on the sector 5 would not be constant, thus making the Dirichlet problem more difficult to solve. For  $\alpha > \alpha_{cr}$  the dependence of  $\phi_s$  on  $z$  is essential and we have given an approximate expression for it in eq.(34). We also argued for the smallness of shock inclination angle,  $\beta \ll 1$ , which simplifies the last expression to the following one

$$\cos \vartheta = \frac{\sqrt{w_0^2 \cos^2 \alpha - 2\phi_s}}{\sqrt{w_0^2 - 2\phi_s}}$$

Note that  $\beta \ll 1$  condition also provides more justification for the constant  $\phi_s$  approximation at  $\alpha < \alpha_{cr}$ . By denoting  $U = 2\phi_s/w_0^2$ , we can rewrite the last expression

$$\cos \vartheta = \frac{\sqrt{\cos^2 \alpha - U}}{\sqrt{1 - U}} = \sqrt{1 - \frac{\sin^2 \alpha}{1 - U}}$$

which relates  $\alpha$  and  $\vartheta$  in a simple way:

$$\sin \alpha = \sqrt{1 - U} \sin \vartheta$$

Considering the case of strong shock reflectivity,  $1 - U \ll 1$ , we see that particle reflection begins at small  $\alpha$ , since  $\sin \alpha_{cr} = \sqrt{1 - U} \ll 1$ . Therefore, we can indeed treat the cross-shock potential as being constant at  $\alpha < \alpha_{cr}$ , that is  $\phi_s \approx \phi_s(\alpha = 0) = \text{const}$ . However,  $\phi_s$  significantly changes in the outflow region on segment 4, above the critical point at  $\alpha_{cr}$ , Fig.8. Using the last relation we can specify the boundary function  $\Psi_5(\vartheta)$ , introduced in Sec.III F. Indeed for the case of  $U \approx 1$ , we have

$$\Psi_5(\vartheta) = \frac{S}{2\pi} \sqrt{1 - U} \sin \vartheta = \Psi_4 \sin \vartheta,$$

in accordance with eq.(44).

The remaining element of the boundary function in the solution  $\Psi(\zeta', 0)$  of the Dirichlet problem given in eq.(47) is the outflow stream function  $\Psi_3$ . Recall that we have chosen this boundary from a mere requirement that the flow is significantly accelerated toward this region as to make the electrostatic potential decreased significantly below its peak at the stagnation point  $x = z = 0$  (see eq.[23]). Since no particles can enter the flow from the shock surface in the segment 3 region, our assumption about the small shock inclination angle,  $\vartheta_s \ll 1$ , holds up. This means that the flow is well aligned with  $z$ - axis, so  $v_x \ll v_z$ . As the flow is irrotational,  $\partial v_z / \partial x \approx 0$ , so we can approximate the stream function by a linear function in  $x$ , or  $\vartheta$ :

$$\Psi_3(\vartheta) = \frac{\pi/2 - \vartheta}{\pi/2 - \vartheta_s} \Psi_4, \quad \text{for } \vartheta_s \leq \vartheta \leq \pi/2$$

This concludes our calculation of the boundary function  $\Psi(\sigma)$  for the Dirichlet solution, given in eq.(47). Two simple functions of the velocity angle  $\vartheta$ ,  $\Psi_3$  and  $\Psi_5$ , obtained above, essentialize the  $\Psi(\sigma)$  variation along the boundary, while  $\Psi(\sigma)$  takes constant values on the remaining boundary segments 1,2 and 4. Expressing  $\vartheta$  in  $\Psi_3$  and  $\Psi_5$  through  $\zeta'$ , using eq.(46), and substituting the result into eq.(47), provide a complete solution for the stream function inside the region of shocked plasma. More difficult, of course, is to convert the  $\vartheta$ - dependence of  $\Psi_3$  and  $\Psi_5$  into  $\zeta$ - dependence and back, as such conversion requires the determination of the Schwartz-Christoffel parameters, as discussed in Appendix B. We defer this task to a future study, as it cannot be completed using only the analytic solutions, to which we adhere in this paper. However, we present below a simplified version of such calculation that can still be completed analytically.

### G. Simple Flow Example

In the preceding subsection, we obtained a general solution for the stream function of the flow between two termination shocks in form of the Poisson integral given by eq.(47). The solution depends on the boundary function  $\Psi$ ,

also specified in Sec.III F. The problem of transforming this result back to the variable  $\sigma$ , that is  $\zeta \mapsto \sigma$ , is not simple, given the complexity of the relation between these two variables shown in eq.(46). In particular, to determine the four parameters of this transform,  $\Theta, \zeta_{1-3}$ , we need to solve four transcendental equations, eqs.(B2-B5). At the same time, the relation between  $\zeta$  and  $\sigma$  variables, established by the Schwartz-Christoffel transform, can be significantly simplified by neglecting some details of the post shock flow. The rationale behind such simplification is as follows.

The boundary function  $\Psi$  rises from zero to its maximum value  $\Psi = \Psi_4$  (reached on segment 4) and back to zero while the contour runs along the segments 3,4, and 5. Let us replace these three connected segments by a single line connecting points  $\sigma = \eta_m + i\pi/2$  and  $\sigma = 0$ . By the principle of analytic continuation, the Poisson integral in eq.(47) will give the same solution inside of the new boundary provided that we know the value of the stream function on this new boundary. Then, we can map it to the appropriate interval on the  $\zeta$ - plane to replace the part of the integral in eq.(47) between  $\zeta = \zeta_3$  and  $\zeta = 0$ . It is clear that the conformal map  $\sigma \mapsto \zeta$  becomes much simpler since the three sides (segments 3-5) replaced by one line specified above. Let us denote by  $\pi\alpha_*$  the angle this line makes with the abscissa on  $\sigma$ - plane:

$$\tan \pi\alpha_* = -\frac{\pi}{2\eta_m} > 0$$

The new conformal map can be written as follows

$$\sigma = \frac{1}{2} \int_0^\zeta \zeta^{-\alpha_*} (1 + \zeta)^{\alpha_* - 1} d\zeta$$

It transforms the semi-strip on  $\sigma$ - plane formed by the line  $\eta_m + i\pi/2$ , 0 and two semi-infinite lines,  $0, +\infty$ ;  $\eta_m + i\pi/2, \infty + i\pi/2$  to the upper half-plane of complex  $\zeta$ . Even better sense of this simplified map one can get by considering the case of small  $|\eta_m| \ll 1$ . As  $\alpha_* \approx 1/2$  in this case the map is simply  $\zeta = \sinh^2 \sigma$  which is easy to check by direct substitution of this relation into the above integral. By rewriting this map in the expanded form

$$\zeta' + i\zeta'' = \frac{1}{2} \cosh 2\eta \cos 2\vartheta - \frac{1}{2} + \frac{i}{2} \sinh 2\eta \sin 2\vartheta,$$

we can change variables in the Poisson integral in eq.(47) and express the solution through  $\vartheta, \eta$  which are directly related to the flow velocity. We also make use of the boundary function  $\Psi(\zeta, 0)$  being non-zero only in the interval  $-1 < \zeta < 0$ . This interval corresponds to the  $0 < \vartheta < \pi/2$  interval on the flow velocity plane. The Poisson integral then rewrites

$$\Psi(\eta, \vartheta) = \frac{2}{\pi} \sinh 2\eta \sin 2\vartheta \int_0^{\pi/2} \frac{\sin 2\vartheta' \Psi(\vartheta', 0) d\vartheta'}{(\cosh 2\eta \cos 2\vartheta - \cos 2\vartheta')^2 + \sinh^2 2\eta \sin^2 2\vartheta'}$$

While being grossly simplified, this expression is helpful for understanding the flow structure in the shocked plasma region. The variable  $\eta$  can be expressed directly through the local velocity  $q$  using eq.(42). The formulas given in Appendix A allows one to map the velocity plane to the physical plane  $x, z$ . Using Bernoulli integral, eq.(23), the flow velocity dependence on  $x, z$  explicitly provides the distribution of the electrostatic potential on the physical plane which is a key ingredient in calculating the growth rate obtained in Sec.4.

#### IV. SUMMARY AND OUTLOOK

In this paper we studied colliding plasmas concentrically flowing from two ohmically exploded wires. Assuming that the flows are mildly supersonic, our main interest was centered around a thin layer of shocked plasma that forms between the colliding flows. We focused on two properties of the layer that can be categorized as microscopic and macroscopic. The microscopic concerns instabilities developing at scales much smaller than the layer itself. Given the anticipated macroscopic characteristics of this plasma, the main candidate is the lower-hybrid drift instability (LHDI), primarily powered by the ExB electron drift. The magnetic field, supporting the drift, is generated at earlier times in the outflow plasmas by currents driven through the wires during their explosion. The ambipolar electric field, which is also needed to produce the drift, emerges from the collision process. This field is also one of the key elements of the macroscopic description of the shocked plasma flow.

Generally, the investigated collision of magnetized plasmas encompasses several elements other than the macroscopic electric field, which are difficult to separate from one another. Before the LHDI sets on, two shocks form that terminate each flow. Oppositely directed magnetic fields are carried toward each other by shocked plasmas and they will eventually reconnect near the mid-plane between the shocks. These processes need to be studied self-consistently, including the LHDI while it provides the anomalous resistivity that, in turn, determines the field reconnection rate in low-collisionality regimes. It is clear, however, that all these phenomena are difficult for studying them self-consistently with mere analytic methods. Therefore, in this paper we addressed the instability and the flow past the shocks independently. This task separation is tenable because we have found the solution of the linear dispersion relation for the instability without imposing specific restrictions on the characteristics of the flow and unstable waves. Such restrictions usually follow from the analysis of macroscopic equilibrium.

For the above-mentioned reasons, our study of the macroscopics of the shocked plasma flow is semi-independent of the instability study. More importantly, the macroscopic consequences of the instability can be included in a form of pondermotive pressure exerted by Lower-hybrid waves on the shocked plasma flow. The main results obtained at this phase of research are the following:

- the growth rate of the lower-hybrid drift instability in the post-shock plasma flow between two exploding wires is calculated in a closed form without further simplifications, customarily applied to similar instability analyses
- the plasma collision process is characterized including the determination of the stand-off distances of the termination shocks formed in the respective flows and the profile of the macroscopic electric field between them
- Chaplygin equations for the flow past the termination shocks are derived using the hodograph map
- general analytic solution for the stream function of the flow is obtained using the Schwartz-Christoffel map of the hodograph plane

These results lay the ground for a more complete characterization of the collision of magnetized plasmas resulting from the wire explosion or otherwise. As the next logical steps they suggest:

- to study macroscopic implications of the LHDI by calculating the electron heating and anomalous resistivity
- to investigate the impact of pondermotive pressure on the flow which was shown to strongly depends on  $T_e/T_i$  ratio
- reiterated consideration of the shocked plasma flow with the LHDI effects included
- study of the magnetic field reconnection in the shocked plasma based on the anomalous resistivity supported by the LHDI
- study of the generation of mesoscale structures resulting from LHDI, ExB shear flow, and field reconnection

The last item is worth commenting briefly as it embodies a wide range of interrelated processes of experimental significance. The importance of the mesoscale structures – which are larger than the lower-hybrid wave length but smaller than the plasma layer – is that they can be probed and visualized by the available laser diagnostics directly [16]. We are planning to explore a number of mechanisms for their generation. These include a spectral transformations to the mesoscale structures from short scale lower-hybrid waves via interactions with acoustic-type perturbations, primarily based on the modulational instability [18]. Other candidates for their formation are the shear flow generated vortices [17], as well as tearing and modulational instabilities in the neutral sheet area [11].

## ACKNOWLEDGMENTS

This work was supported by the Air Force Office of Scientific Research under grant LRIR # 16RYCOR289. Public release approval record: 88ABW-2018-4241

## Appendix A: Hodograph Transform

We use that particular type of hodograph transform in which the role of the new dependent variables is assumed by the flow potential and the stream function, eqs.(25) and (35), while the role of the independent variables is left for the velocity components. By definition, the flow potential  $\chi$  and stream function  $\psi$  obey the following relations

$$\begin{aligned}d\chi &= v_x dx + v_z dz \\d\psi &= -v_z \rho dx + v_x \rho dz\end{aligned}$$

from which we obtain

$$\begin{aligned}dx &= \frac{\cos \vartheta}{q} d\chi - \frac{\sin \vartheta}{\rho q} d\psi \\dz &= \frac{\cos \vartheta}{\rho q} d\psi + \frac{\sin \vartheta}{q} d\chi\end{aligned}$$

Here and below we use the cylindrical coordinates in the velocity space  $q$  and  $\vartheta$  introduced in eq.(36). The last two equations manifest  $dx$  and  $dz$  as complete differentials of functions  $x(\chi, \psi)$  and  $z(\chi, \psi)$ . The respective cross-derivatives of the coefficients at  $d\chi$  and  $d\psi$  must then be equal:

$$\begin{aligned}\frac{\partial}{\partial \psi} \frac{\cos \vartheta}{q} &= -\frac{\partial}{\partial \chi} \frac{\sin \vartheta}{\rho q} \\ \frac{\partial}{\partial \psi} \frac{\sin \vartheta}{q} &= \frac{\partial}{\partial \chi} \frac{\cos \vartheta}{\rho q}\end{aligned}$$

This system of equations can be rewritten as follows

$$\begin{aligned}\left[ \frac{\partial}{\partial \chi} \frac{1}{\rho q} - \frac{1}{q} \frac{\partial \vartheta}{\partial \psi} \right] \sin \vartheta + \left[ \frac{\partial}{\partial \psi} \frac{1}{q} + \frac{1}{\rho q} \frac{\partial \vartheta}{\partial \chi} \right] \cos \vartheta &= 0 \\ \left[ \frac{\partial}{\partial \chi} \frac{1}{\rho q} - \frac{1}{q} \frac{\partial \vartheta}{\partial \psi} \right] \cos \vartheta - \left[ \frac{\partial}{\partial \psi} \frac{1}{q} + \frac{1}{\rho q} \frac{\partial \vartheta}{\partial \chi} \right] \sin \vartheta &= 0\end{aligned}$$

The terms in the brackets may be regarded as two unknown entering a linear system of two equations. Since the determinant of this system is  $\sin^2 \vartheta + \cos^2 \vartheta = 1$ , it has only a trivial solution. In other words, each term in the brackets must be zero. Substituting  $\rho$  from eq.(39), we write these two conditions as follows:

$$\begin{aligned}\frac{\partial \vartheta}{\partial \psi} &= \frac{q^2 - 1}{\rho q} \frac{\partial q}{\partial \chi} \\ \frac{\partial \vartheta}{\partial \chi} &= \frac{\rho}{q} \frac{\partial q}{\partial \psi}\end{aligned}$$

By swapping the dependent and independent variables in these equations, we obtain Chaplygin eqs.(37-38). The inversion of the derivatives in these equations can be achieved by writing identities of the following kind

$$\frac{\partial \vartheta}{\partial \psi} = \frac{\partial(\vartheta, \chi)}{\partial(\psi, \chi)} = \frac{\partial(\vartheta, q)}{\partial(\psi, \chi)} \frac{\partial(\psi, \chi)}{\partial(\vartheta, q)} = J \frac{\partial \chi}{\partial q}$$

where the Jacobian of the transform between the two sets of variables is

$$J = \frac{\partial(\vartheta, q)}{\partial(\psi, \chi)}.$$

## Appendix B: Schwartz-Christoffel transform

The Schwartz-Christoffel transform maps a polygon on a complex plane to the upper half of a new plane. In our case we need to map the pentagon on the  $\sigma = \eta + i\vartheta$ - plane shown in Fig.8 (right panel) to the upper half-plane of the complex plane  $\zeta$ . The four right angles of the pentagon at the finite points of  $\sigma$ - plane will correspond to four

finite points of the real  $\zeta$ - axis:  $\zeta_3 < \zeta_2 < \zeta_1 < 0$ , while the two points at  $\eta = \infty$  are considered as one zero-degree angle of the pentagon, as indicated in Sec.III F. As we know from the complex analysis, an integral of the kind

$$\sigma = \Theta \int_{\zeta_0}^{\zeta} (\zeta - \zeta_1)^{\alpha_1/\pi-1} \dots (\zeta - \zeta_n)^{\alpha_n/\pi-1} \quad (\text{B1})$$

maps a polygon with  $n$  angles on the  $\sigma$ - plane to the upper half-plane  $\eta$ . Here the constants  $\alpha_k$  are the internal angles of the polygon. According to the point-to-point correspondence list (1-6) in Sec.III F, we can specify the anchor points  $\zeta_k$  and angles  $\alpha_k$  to obtain the expression for  $\sigma$  shown in eq.(46):

$$\sigma = \Theta \int_0^{\zeta} \sqrt{\frac{\zeta - \zeta_1}{(\zeta - \zeta_2)(\zeta - \zeta_3)(1 - \zeta)\sqrt{\zeta}}}$$

Apart from preserving the origin ( $1/\sqrt{\zeta}$  factor in the integrand), this choice of the transform parameters  $\zeta_k, \alpha_k$  connects, in particular, the  $\zeta = 1$  pole to the zero-angle point of the pentagon on the right panel of Fig.8. The remaining  $\zeta_{1-3}$  anchor points correspond to the two  $\pi/2$  angles and one  $3\pi/2$  angle of the pentagon. The integral thus maps the interval  $\zeta_1 < \zeta < 0$  to the interval of the imaginary  $\sigma$ - axis,  $0 < \Im\sigma < \pi/2 - \vartheta_s$ . The branch of  $\sqrt{\zeta}$  is such that  $\sqrt{\zeta} > 0$  for  $\zeta > 0$ . The remaining two finite sides of the pentagon are mapped from the intervals  $(\zeta_2, \zeta_1)$  and  $(\zeta_3, \zeta_2)$ . The two semi-infinite sides of the pentagon are related to the point  $\zeta = 1$  with  $\arg(1 - \zeta) = 0, \pi$ . The transition from the lower to upper branch occurs when the contour on  $\zeta$ - plane goes over the  $\zeta = 1$  pole. As the  $\Im\sigma$  jumps from 0 to  $\pi/2$ , we have the following relation for the parameters of the Schwartz-Christoffel integral:

$$\Theta \sqrt{\frac{1 - \zeta_1}{(1 - \zeta_2)(1 - \zeta_3)}} = \frac{1}{2} \quad (\text{B2})$$

The contour then goes to  $\Re\zeta = \infty$ , and the closing arc  $|\zeta| = \infty$  is therefore mapped to some point on the upper semi-infinite branch, yielding no further relation for the parameters of the map. By requiring that the integrals between the remaining points  $\zeta_{1-3}$ , including the origin, produce the appropriate changes in  $\sigma$ , as listed under the items (1-6) in Sec.III F, we find the following relations

$$\vartheta_s = \Theta \int_{\zeta_3}^{\zeta_2} \sqrt{\frac{\zeta - \zeta_1}{(\zeta_2 - \zeta)(\zeta - \zeta_3)(1 - \zeta)\sqrt{\zeta}}} \quad (\text{B3})$$

$$\eta_m = -\Theta \int_{\zeta_2}^{\zeta_1} \sqrt{\frac{\zeta - \zeta_1}{(\zeta - \zeta_2)(\zeta - \zeta_3)(1 - \zeta)\sqrt{\zeta}}} \quad (\text{B4})$$

$$\frac{\pi}{2} - \vartheta_s = \Theta \int_{\zeta_1}^0 \sqrt{\frac{\zeta - \zeta_1}{(\zeta - \zeta_2)(\zeta - \zeta_3)(1 - \zeta)\sqrt{-\zeta}}} \quad (\text{B5})$$

Eqs.(B2-B5) are thus four equations for four Schwartz-Christoffel parameters  $\Theta, \zeta_{1-3}$ , given the flow region boundaries described here by the two values of  $\eta_m$  and  $\vartheta_s$ .

- 
- [1] J. P. Chittenden. The effect of lower hybrid instabilities on plasma confinement in fiber Z pinches. *Physics of Plasmas*, 2:1242–1249, April 1995.
- [2] J. P. Chittenden, S. V. Lebedev, S. N. Bland, F. N. Beg, and M. G. Haines. One-, two-, and three-dimensional modeling of the different phases of wire array Z-pinch evolution. *Physics of Plasmas*, 8:2305–2314, May 2001.
- [3] R. C. Davidson and N. T. Gladd. Anomalous transport properties associated with the lower-hybrid-drift instability. *Physics of Fluids*, 18:1327–1335, October 1975.

- [4] M. E. Dieckmann, D. Doria, G. Sarri, L. Romagnani, H. Ahmed, D. Folini, R. Walder, A. Bret, and M. Borghesi. Electrostatic shock waves in the laboratory and astrophysics: similarities and differences. *Plasma Physics and Controlled Fusion*, 60(1):014014, January 2018.
- [5] R.P. Drake. *High Energy Density Physics*. Graduate Texts in Physics Series. Springer-Verlag, 2018.
- [6] A. V. Gurevich. Distribution of Captured Particles in a Potential Well in the Absence of Collisions. *Soviet Journal of Experimental and Theoretical Physics*, 26:575, March 1968.
- [7] N. K.-R. Kevlahan. The vorticity jump across a shock in a non-uniform flow. *Journal of Fluid Mechanics*, 341:371–384, June 1997.
- [8] L. D. Landau and E. M. Lifshitz. *Fluid Mechanics*. Pergamon Press, 1987.
- [9] P. C. Liewer and N. A. Krall. Self-consistent approach to anomalous resistivity applied to theta pinch experiments. *Physics of Fluids*, 16:1953–1963, November 1973.
- [10] M. A. Malkov, R. Z. Sagdeev, G. I. Dudnikova, T. V. Liseykina, P. H. Diamond, K. Papadopoulos, C.-S. Liu, and J. J. Su. Ion-acoustic shocks with self-regulated ion reflection and acceleration. *Physics of Plasmas*, 23(4), 2016.
- [11] M. A. Malkov and V. I. Sotnikov. Lower hybrid drift instability and reconnection of magnetic lines of force. *Soviet Journal of Plasma Physics*, 11:1096–1105, #sep# 1985.
- [12] S. S. Moiseev and R. Z. Sagdeev. Collisionless shock waves in a plasma in a weak magnetic field. *Journal of Nuclear Energy*, 5:43–47, January 1963.
- [13] Note that in the case of the equivalent colliding flow configuration, the role of reflected ions is taken by the ions from the opposite flow.
- [14] D. D. Ryutov, N. L. Kugland, M. C. Levy, C. Plechaty, J. S. Ross, and H. S. Park. Magnetic field advection in two interpenetrating plasma streams. *Physics of Plasmas*, 20(3):032703, March 2013.
- [15] R. Z. Sagdeev. Cooperative Phenomena and Shock Waves in Collisionless Plasmas. *Reviews of Plasma Physics*, 4:23–+, 1966.
- [16] G. S. Sarkisov, S. E. Rosenthal, K. R. Cochrane, K. W. Struve, C. Deeney, and D. H. McDaniel. Nanosecond electrical explosion of thin aluminum wires in a vacuum: Experimental and computational investigations. *Phys. Rev. E*, 71(4):046404, April 2005.
- [17] V. I. Sotnikov, J. N. Leboeuf, and S. Mudaliar. Scattering of Electromagnetic Waves in the Presence of Wave Turbulence Excited by a Flow With Velocity Shear. *IEEE Transactions on Plasma Science*, 38:2208–2218, September 2010.
- [18] V. I. Sotnikov, V. D. Shapiro, and V. I. Shevchenko. Macroscopic consequences of collapse at the lower hybrid resonance. *Fizika Plazmy*, 4:450–459, March 1978.
- [19] L. G. Suttle, J. D. Hare, S. V. Lebedev, A. Ciardi, N. F. Loureiro, G. C. Burdiak, J. P. Chittenden, T. Clayson, J. W. D. Halliday, N. Niasse, D. Russell, F. Suzuki-Vidal, E. Tubman, T. Lane, J. Ma, T. Robinson, R. A. Smith, and N. Stuart. Ion heating and magnetic flux pile-up in a magnetic reconnection experiment with super-Alfvénic plasma inflows. *Physics of Plasmas*, 25(4):042108, April 2018.